Materials Advances

Accepted Manuscript

This article can be cited before page numbers have been issued, to do this please use: L. Quigley, N. A. Bhatt, K. Evancho, J. Shen, J. Lu, C. A. Mihalko, J. P. Barnard, M. Chhabra, P. Lu, R. Sarma, A. Siddiqui and H. Wang, *Mater. Adv.*, 2026, DOI: 10.1039/D5MA01163A.

ROYAL SOCIETY OF CHEMISTRY

rsc.li/materials-advances

View Article Online
DOI: 10.1039/D5MA01163A

Data Availability

The data supporting this article have been included as part of the Supplementary Information.

View Article Online
DOI: 10.1039/D5MA01163A

Tailored Magnetic Properties in CoFeB-$BiFeO_3$ Nanocomposite Thin Films

Lizabeth Quigley,[1] Nirali A. Bhatt,[1] Katrina Evancho,[1] Jianan Shen,[1] Juanjuan Lu,[1] Claire A. Mihalko,[1] James P. Barnard,[1] Max Chhabra,[1] Ping Lu,[2,3] Raktim Sarma,[2, 3] Aleem Siddiqui,[2] Haiyan Wang[1, 4 *]

[1] School of Materials Engineering, Purdue University, West Lafayette, Indiana 47907, USA

[2] Sandia National Laboratories, Albuquerque, New Mexico 87185, USA

[3] Center for Integrated Nanotechnologies, Sandia National Laboratories, Albuquerque, New Mexico 87185, USA

[4] School of Electrical and Computer Engineering, Purdue University, West Lafayette, Indiana 47907, USA

*Corresponding Author: hwang00@purdue.edu

View Article Online
DOI: 10.1039/D5MA01163A

Abstract

Ferromagnetic CoFeB (CFB) and multiferroic $BiFeO_3$ (BFO) are both widely studied materials for thin film device applications and are previously implemented in multilayer or bilayer stacks. In this work, we demonstrate for the first time particle-in-matrix (PiM) films as a new CFB-BFO nanocomposite form. Two PiM films were deposited under nitrogen and vacuum atmospheres and compared against a more typical bilayer system. The different deposition conditions lead to microstructure tuning of the PiM films, with the two displaying inverted microstructures. The PiM films also displayed a large increase in the saturation magnetization compared to the bilayer film and slightly enhanced antiferromagnetic-ferromagnetic exchange coupling out-of-plane. All three films displayed ferroelectric properties, with the PiM film deposited under a nitrogen atmosphere showing significant leakage. These CFB-BFO nanocomposites present potential for future multiferroic device applications.

Keywords:

CFB (CoFeB), BFO ($BiFeO_3$), thin films, magnetic properties, exchange coupling, particle-in-matrix, nanocomposites

View Article Online
DOI: 10.1039/D5MA01163A

Introduction

Novel multiferroic materials enable new applications in devices by combining both ferromagnetic and ferroelectric properties into one structure, often allowing for stronger properties than either single material by itself.[1–5] Some applications of these materials include ferroelectric random access memory (FeRAM) and ferroelectric spintronics, depending on which ferromagnetic and ferroelectric material is selected.[6–11] One ferromagnetic material suited for these applications, among others, is CoFeB (CFB). CFB is a soft ferromagnetic material commonly used in magnetic tunnel junctions (MTJs) for magnetic memory and has a low magnetic damping for spintronic applications.[12–20] While CFB is not ferroelectric, it is metallic in nature and thus conducting, allowing it to work as a charge-conducting layer.[21] For its current applications, CFB is often grown in multilayer stacks, usually with MgO, an insulator that acts as a tunnel barrier in MTJs.[15,16,22–24] Prior work has shown that $BiFeO_3$ (BFO) has emerged as an alternative in tunnel barrier applications with the added bonus of being ferroelectric, allowing this material to work with CFB in future multiferroic applications, particularly FeRAM.[25–31] While BFO does not provide nearly an equivalent tunneling magnetoresistance as MgO (30% to 600%), studies of a CFB-BFO system have not been considered.[32,33] BFO introduces a ferroelectric phase, which MgO cannot due to its insulating nature, allowing for potential regulation of the magnetic states through electric fields. In addition, BFO is a perovskite and also known as one of the single-phase multiferroic materials, also exhibiting weak antiferromagnetic properties.[25,27,28,30] The ferroelectric polarization occurs due to Bi^{+3} in the A site while the antiferromagnetic properties occurs from Fe^{3+} in the B site of the perovskite crystal structure.[25] This provides an advantage for future nanocomposites made of CFB-BFO in the form of antiferromagnetic-ferromagnetic exchange coupling, leading to increased film coercivity when compared to just CFB or BFO alone.[34,35] Work has also been done to examine

View Article Online
DOI: 10.1039/D5MA01163A

BFO's ability to work in spintronic devices, showing yet again that these two materials are compatible in their future applications.[36]

Conventional designs for multiferroics rely on bilayers or multilayer stacks. The benefit of this layered deposition method is the introduction of lateral interfaces between each of the deposited layers. The in-plane strain introduced by the layers also allows for property tuning of the film by affecting the growth of the next layer.[37] However, this method requires the switching between the two different material targets for each new layer to be deposited, increasing deposition time and complexity, especially if done using pulsed laser deposition (PLD). The layered structures are typically achieved through sputter deposition, which is well established for industry applications due to its high throughput and deposition area coverage. Also due to the reliable nature of the sputter deposition, most magnetoresistive devices are made with sputtering methods.[38] As an alternative, particle-in-matrix (PiM) nanocomposites, films with nanoparticles of one material embedded within a matrix of another, are co-deposited through a one-step process. PiM films also allow for tunable composition through adjustment of the deposition parameters, further leading to tuned properties.[39,40] There is also an increase in material interfaces in PiM films due to the high surface area of the embedded nanoparticles. The amount of interaction between particles and the matrix depends on the density of the two phases and the size of the nanoparticles, with smaller, more densely spaced nanoparticles having more interactions.[41]

In this work, three CFB-BFO nanocomposites thin films were deposited using PLD: two PiM nanocomposites deposited under different atmospheres (one under a Nitrogen partial pressure, the other under Vacuum), and a more conventional Bilayer film. The Bilayer film first had the CFB layer deposited followed by the BFO layer. The schematics of these three films can be found in Figures 1A1-A3, and detailed deposition methods can be found in the Experimental Section.

View Article Online
DOI: 10.1039/D5MA01163A

Previous literature has not reported the deposition of CFB-BFO nanocomposites, allowing for this to be a novel demonstration. Reference Pure CFB and Pure BFO films were also deposited and can be found in Supplementary Figures S2-S4. After deposition, the material and structure of the films were characterized with X-ray diffraction (XRD), transmission electron microscopy (TEM), scanning transmission electron microscopy (STEM) and energy dispersive x-ray spectroscopy (EDS). The magnetic hysteresis loops (M vs. H) and electrical hysteresis loops (P vs. E) of each film were then measured to see how the microstructures differed and affected the properties of the films, with the electrical measurement results located in the Supplementary Data.

View Article Online
DOI: 10.1039/D5MA01163A

Results & Discussion

The crystalline phase and orientation of the two particle-in-matrix (PiM) films, deposited under nitrogen and vacuum conditions, were characterized and compared to that of the Bilayer film using x-ray diffraction (XRD), as seen in Figure 1B. Figures 1A1-1A3 show a schematic drawing of each of the deposited films based on the microstructure seen in the transmission electron microscopy (TEM) imaging the Figure 2 below. All three films displayed the CoFeB (CFB) (*220*) orientation, showing that this is the preferred (*220*) texture for CFB growth. Indeed, for the Nitrogen PiM film, the CFB (*220*) orientation is the only CFB phase, showing higher growth orientations compared to the two other films with multiple CFB orientations. In the Vacuum PiM film, the CFB (*220*) peak has a higher intensity over the other grown CFB orientation, (*020*). The higher CFB phase purity in the Nitrogen PiM film may have resulted from the nitrogen partial pressure atmosphere allowing the CFB plasma plume to fully develop, influencing the growth's kinetic energies. In vacuum, this effect is minimized, and the plasma plume size is minimized leading to less optimum CFB growth.

In the Bilayer film, deposited as a more conventional microstructure for direct microstructure and property comparison with the PiM films, multiple CFB phases occurred, despite the deposition also being done under a nitrogen partial pressure. This would suggest that CFB is not an optimal material to grow directly on STO with PLD, supported by the growth rate of the material which is 1.33×10^{-3} nm/pulse, calculated from the Bilayer film's growth. The decrease in CFB phases seen in the PiM films suggests that the co-deposition with $BiFeO_3$ (BFO) leads to preferential growth of CFB compared to direct growth of CFB by itself on STO. Due to the metallic nature of CFB nature, it can be assumed that it would grow in an island growth mode, further supported by the TEM results discussed in Figure 2, resulting in the multiple orientations

View Article Online
DOI: 10.1039/D5MA01163A

seen in the XRD data.[42] In these instances, co-deposition with another material allows for easier growth of these films. For all three samples, pseudocubic BFO peaks were observed as shoulder peaks on the STO substrate peaks, with no significant differences between the films, showing that the BFO phase grew well in all the deposition conditions. Further analysis of the CFB and BFO phases was performed through in-plane phi scans, shown in Supplementary Figure S1. Scans were conducted in the CFB (*110*) and STO (*110*) orientations, with the STO scan potentially overlapping the BFO phase due to their close lattice parameters, as seen in Figure 1. All of the phi scans show the BFO phase with four-fold symmetry, indicating its pseudocubic crystal structure.[28,30] In all three scans, the CFB phase has two wide peaks spanning the width of two STO phi scan peaks, showing a weaker preference for in-plane symmetry than the out-of-plane orientation.

View Article Online
DOI: 10.1039/D5MA01163A

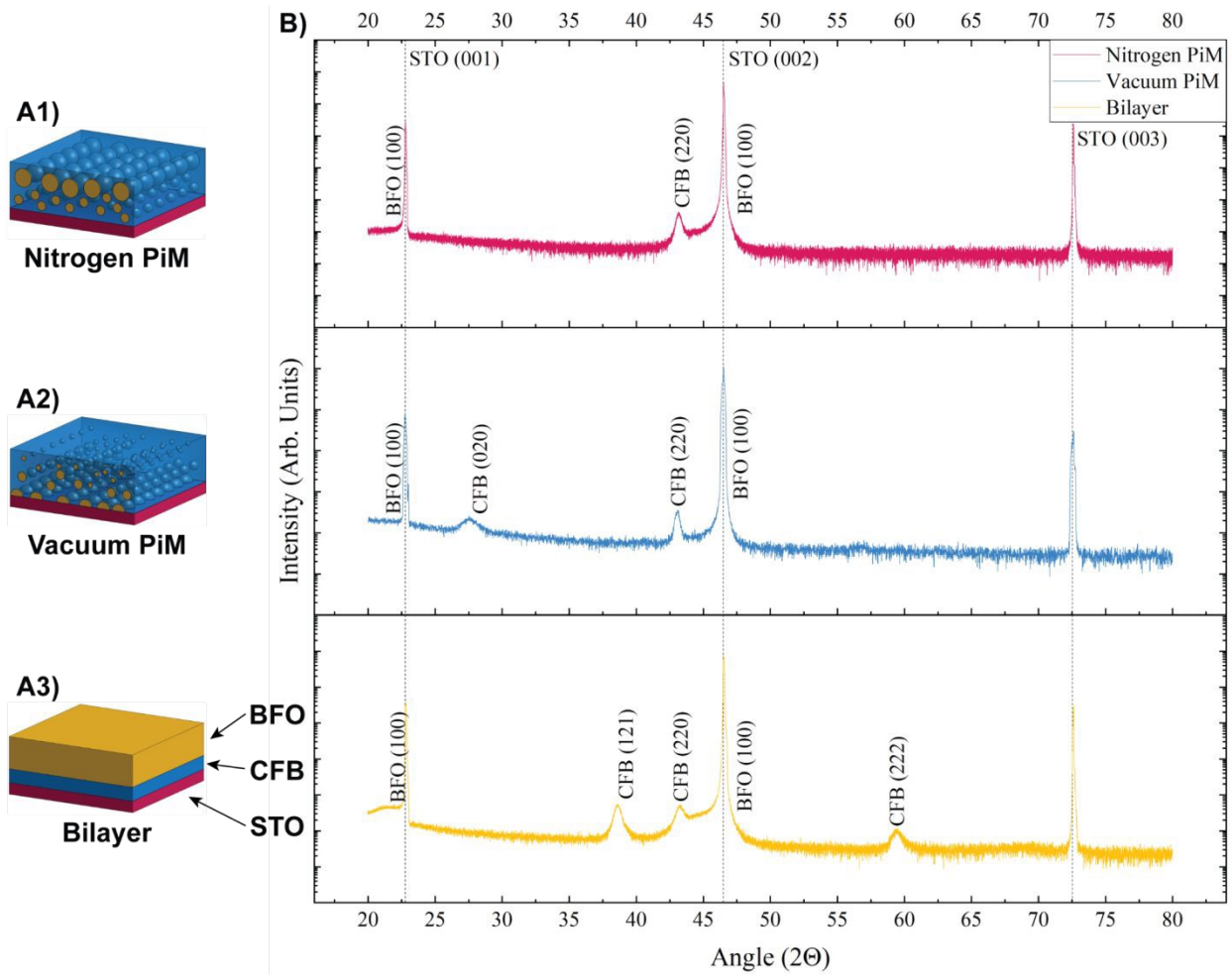

Figure 1: Schematics for the A1) Nitrogen PiM, A2) Vacuum PiM, and A3) Bilayer films with labeling for the color coding of the schematics. B) XRD θ-2θ of the three films.

Further microstructural characterization of the films was performed through TEM, scanning transmission electron microscopy (STEM), and energy-dispersive x-ray spectroscopy (EDS) imaging, as shown in Figure 2. The Nitrogen PiM film (Figures 2A1-A5) shows a film with a preference for large BFO particle growth near the top of the film, though some smaller BFO particles are distributed throughout the lower half of the film, showing that CFB formed as the matrix in these films. This is most apparent from the STEM image and corresponding EDS map in Figures 2A2 and 2A3. Despite the preference for BFO particle growth at the top of the film,

View Article Online
DOI: 10.1039/D5MA01163A

Figure 2A3 shows significant yellow Bi below the substrate because this was the only film to show Bi- diffusion into the STO substrate. A low-magnification TEM image of the film (Figure 2A4) confirmed that the observed microstructure is uniform across the film and not limited to the area selected for EDS analysis. In the TEM images, an amorphous glue layer is visible at the top of the film, resulting from sample preparation for the TEM sample, but examination of the EDS map shows that this is not part of the film. The higher-resolution image in Figure 2A5 indicated the BFO phases through Moiré patterns, suggesting a misalignment between the CFB and BFO phases under these deposition conditions.

Regarding the Vacuum PiM film (Figures 2B1-B5), an inverted microstructure relative to the Nitrogen PiM film was revealed. As shown in the STEM image and corresponding EDS map in Figures 2B2 and 2B3, the larger BFO nanoparticles are more heavily distributed along the substrate, with the smaller nanoparticles distributed in the upper half of the film, and with CFB again forming the matrix. However, the overall distribution of BFO nanoparticles throughout the film is more consistent, with some areas having nanoparticles stacked on top of each other. The low-magnification TEM image (Figure 2B4) again shows that the microstructure stays consistent throughout the imaged area. Brighter and darker contrast regions in this image were distributed to preferential ion milling and not differences in material composition. To ensure this, in the STEM image and corresponding EDS map, both a brighter and darker area were included and have a consistent microstructure. Unlike the Nitrogen PiM film, the high-resolution image in Figure 2B5 showed a lack of Moiré patterns, suggesting improved alignment between the CFB and BFO phases.

Finally, the Bilayer film (Figures 2C1-C5), where CFB was deposited first and BFO second, the STEM and corresponding EDS map in Figures 2C2 and 2C3 reveal unexpected BFO

View Article Online
DOI: 10.1039/D5MA01163A

diffusion through the CFB layer along the STO substrate. This was likely enabled by the discontinuous nature of the CFB layer allowing for easier diffusion of the BFO phase. However, the uniform thickness of the CFB Flayer supports some continuity of the CFB layer overall during growth, such as similar surface energies during deposition. The low-magnification image (Figure 2C4) is used to support the consistency of this microstructure, especially the thin layer of BFO below the CFB layer and the discontinuity of the CFB layer. The last high-resolution image in Figure 2C5 shows BFO grows well both above and below the CFB layer. The CFB layer is crystalline in the TEM images, which is also evidenced by its peaks in the XRD in Figure 1, but this is not as apparent in the TEM image. This difference seen in the crystallinity could help explain the broad peaks seen in the phi scans for the CFB phase in Supplementary Figure S1. In Supplementary Figure S5 the O- and Fe- maps for all films are included, except B- as it is not easily identifiable by EDS. The formation of the CFB matrix phase for the two PiM films suggests that the co-deposition of the CFB and BFO phases results in better material composition, possibly leading to better magnetic properties due to the increased ferromagnetic CFB phase. Supplementary Table S1 reports the thickness of all the films, including the Pure CFB and Pure BFO films.

View Article Online
DOI: 10.1039/D5MA01163A

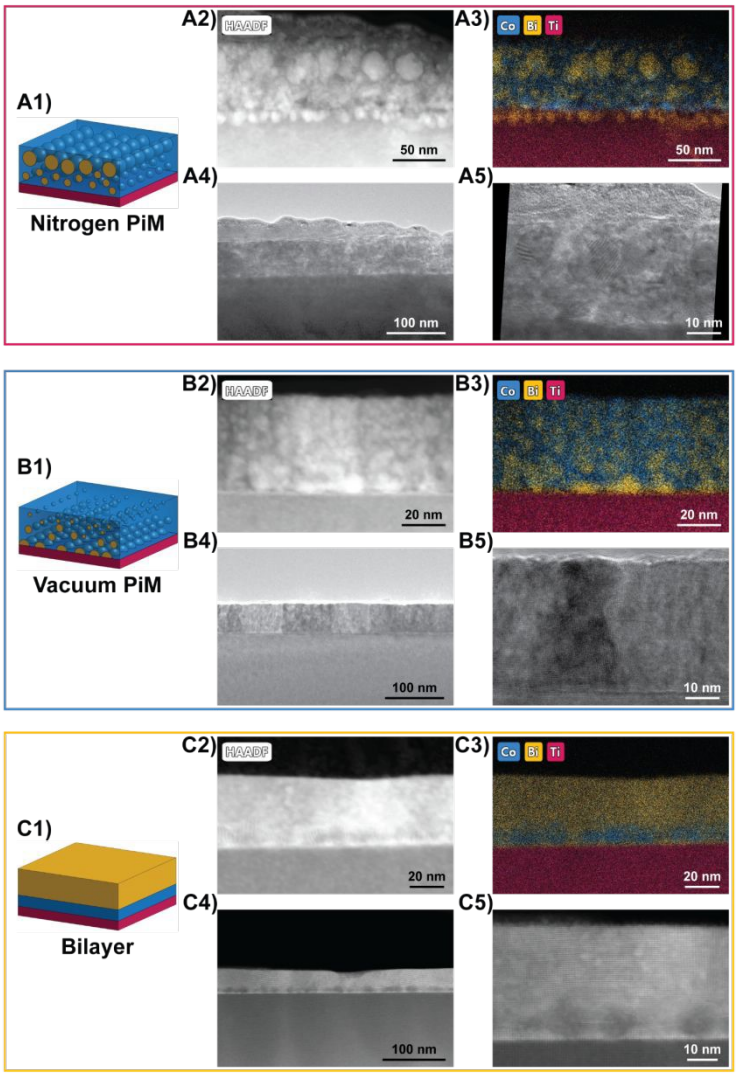

Figure 2: A) The Nitrogen PiM Film, B) The Vacuum PiM Film, and C) The Bilayer Film. 1) Schematic drawing, 2) STEM image for the corresponding EDS map, 3) EDS map showing Co-, Bi-, and Ti-, 4) Low-magnification TEM image of the film, 5) High-resolution image showing the film interface.

Considering the potential magnetic properties in the films, magnetic hysteresis loops were measured and are shown in Figure 3. These measurements were performed at both 300 K and 10 K for all three CFB-BFO nanocomposite films. Both PiM films displayed a large increase in saturation magnetization compared to the Bilayer film. A table of the saturation magnetization and coercive field for all films and each temperature can be found in Supplementary Table S2. This

View Article Online
DOI: 10.1039/D5MA01163A

includes the values for the Pure CFB and Pure BFO films. The saturation for the Pure CFB film is significantly weaker than values traditionally seen in literature, which is a result of the suboptimal CFB deposition seen during growth on STO through PLD, as explained in the XRD results in Figure 1 here. Supplementary Figure S4 includes the hysteresis loops for pure BFO and CFB films as reference. The PiM films also exhibited stronger out-of-plane (OP) saturation magnetization compared to the in-plane (IP), while the Bilayer film had both orientations as equivalent. This orientation preference in the PiM film is attributed to the microstructure allowing for more anisotropy.[43]

Observing the coercivity of the films, at 300 K, all films measured below 2 kOe, and in most instances, the Bilayer film showed a larger coercivity than the PiM films. One exception is seen in the inset in Figure 3A, with the OP orientation of the Vacuum PiM film. At 10 K, the Bilayer film has the largest coercivity, as seen in the inset in Figure 3B. The reason for this effect at 300 K is likely due to the microstructure of each film. In the Vacuum PiM film, the distribution of CFB throughout the film thickness allows for enhancement of the OP magnetic response. In the Nitrogen PiM film, the large BFO nanoparticles near the top of the film act almost like the top BFO layer of the Bilayer film, minimizing the thickness of the CFB layer. However, the CFB matrix still allows for growth in a three-dimensional manner, allowing for the film's OP coercivity to be larger than its IP coercivity, but not larger than that of the Bilayer film. The fact that both PiM films show a preference for OP anisotropy over IP supports their increased anisotropy over the Bilayer film. This increase in magnetic saturation could also be due to the improved growth of the CFB phase and more ferromagnetic CFB in the overall film. Due to the Bilayer film having a consistent IP and OP coercivity, it is safe to assume that the increase coercivity at 10 K is not due to perpendicular magnetic anisotropy that can occur in other CFB stack systems.[44]

View Article Online
DOI: 10.1039/D5MA01163A

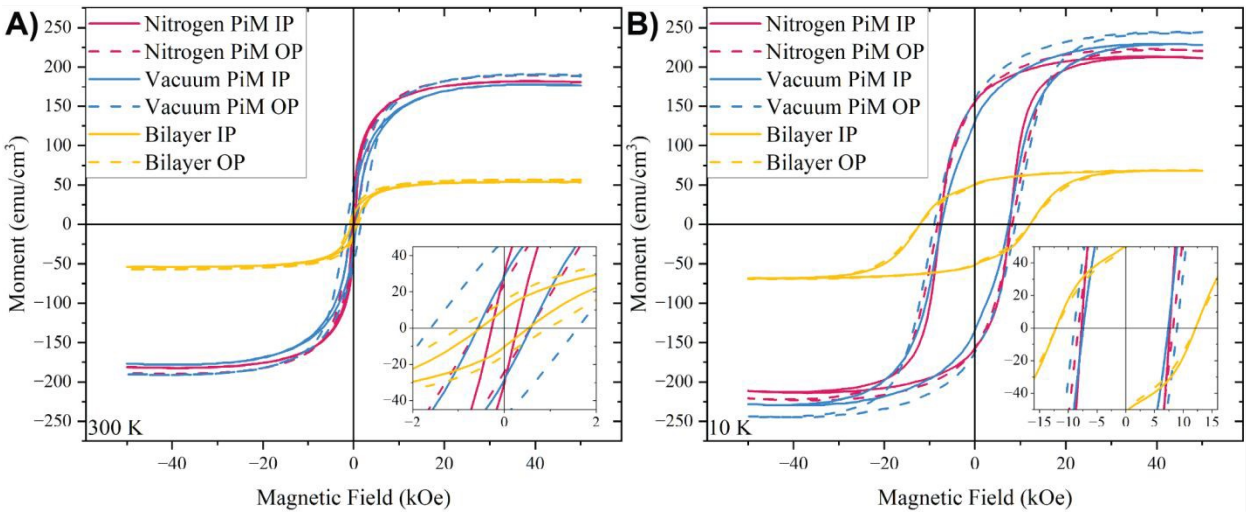

Figure 3: Magnetic hysteresis (M vs. H) data showing both in-plane (IP) and out-of-plane (OP) orientations for all films at A) 300 K and B) 10 K, zero-field cooled.

Instead, exchange coupling between the antiferromagnetic BFO and ferromagnetic CFB is expected for the nanocomposite films. To confirm this, magnetic hysteresis loops were measured at 10 K after field cooling (FC) under ±10, ±20, and ±30 kOe. These measurements were performed on all three films in the OP direction with a more detailed explanation in the Experimental Methods. The OP orientation was chosen for these measurements to highlight the strength of the nanocomposite design as previous work performed with the co-deposited nanocomposite design has shown a stronger exchange bias in the OP orientation.[45] The resulting hysteresis loops of each measurement can be found in Supplementary Figure S6. Figure 4A shows H_{EB}, the exchange bias field or the shift of the hysteresis loop along the magnetic field axis, for each sample as an effect of the applied field during cooling. The corresponding values are listed in Supplementary Table S3, along with the average coercive field (H_C) and the saturation magnetization. The clear shift seen from the zero-field cooled (ZFC) to the FC states

View Article Online
DOI: 10.1039/D5MA01163A

supports the presence of exchange coupling. Another clear indicator of exchange coupling is the negative H_{EB} after positive FC and a positive H_{EB} after negative FC. At an applied cooling field of ±10 kOe the two PiM films have a larger H_{EB} than the Bilayer film suggesting that this nanocomposite design enhanced the magnetic interface coupling due to increased surface area between the antiferromagnetic BFO and ferromagnetic CFB. The asymmetry seen between the positive and negative H_{EB} is attributed to incomplete spin relaxation. Measurements were performed in an MPMS3, and were heated to 400 K between measurements which is insufficient to fully demagnetize the BFO phase with a Néel temperature of ~640 K.[27–29,31] As explained in the Experimental Methods, between each of the different sets of fields, the samples were heated to above the Néel temperature.

Upon doing the field cooled measurements with the higher applied fields, the Bilayer sample did not display the lowest H_{EB}. Instead, the Vacuum PiM film, on average, displayed the lowest exchange bias. However, looking at the hysteresis loops in Supplementary Figure S6A-C and the average saturation, graphed in Figure 4B and listed in Supplementary Table S3, the saturation magnetization of the sample further increased at the higher applied cooling fields. So, while the exchange bias decreased, the increased saturation of the sample still supports the nanocomposite film experiencing greater AFM-FM exchange coupling than the Bilayer film, due to increased interfaces between CFB and BFO. The Nitrogen PiM film does not experience this secondary shift in the coercivity but continues to have a greater H_{EB} than the Bilayer film except for at the -30 kOe applied cooling field measurement. Due to the H_{EB} values being 0.1 kOe apart from each other, as seen in Supplementary Table S3, and the negative applied fields experiencing incomplete spin relaxation, this effect can be assumed to be minor and that the Nitrogen PiM film experiences overall greater exchange bias than the Bilayer film. As seen in Supplementary Figure

View Article Online
DOI: 10.1039/D5MA01163A

S6D, magnetic moment versus temperature measurements (i.e., M vs. T curves) were also conducted for these three films to determine if they showed a ferromagnetic response and if there were any effects from the suspected oxygen defects in the BFO phase. Exact details of this measurement can be found in the Experimental Methods, and the measurement temperature range was 8-400 K. Oxygen vacancies in BFO, and materials like it, can weaken indirect exchange or introduce frustrated or weakly interacting regions, particularly with the Fe-O-Fe bonds, as previously reported.[46] This vacancy-induced magnetic phase softening and spin-glass behavior can be seen in Supplementary Figure S6D, supporting the growth of oxygen vacancies in the BFO phase. It can also be seen that these three films' responses follow a pattern based on their film thickness, reported in Supplementary Data Table S1. The Vacuum PiM and Bilayer films with comparable thickness have very similar responses in this graph, while the thicker Nitrogen PiM has a stronger response at all temperatures.

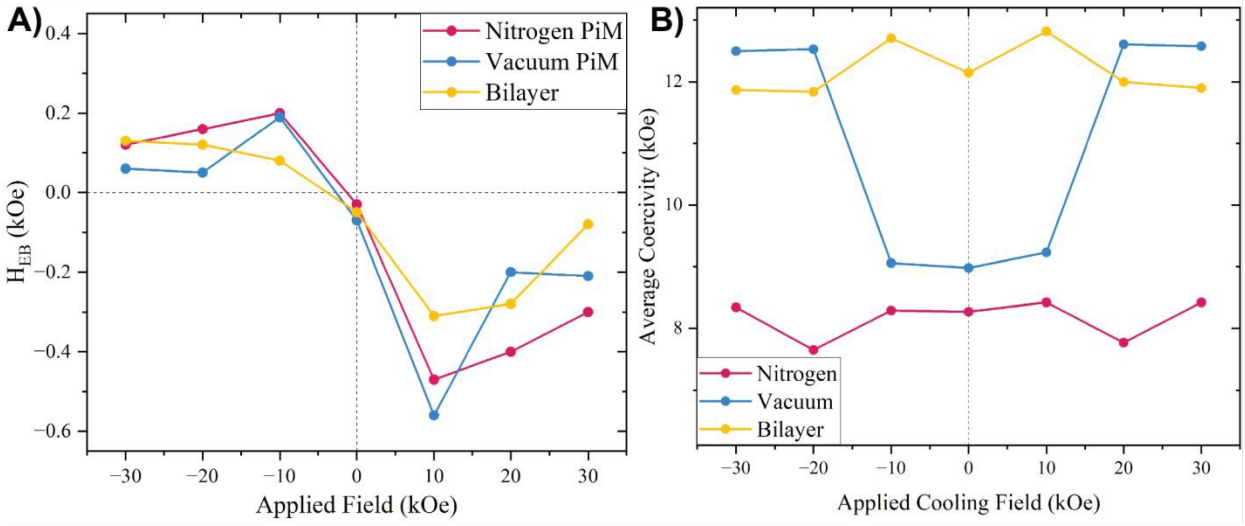

Figure 4: A) Graph shown H_{EB} versus field applied during cooling. B) The average coercivity for the three films after the zero-field cooled and applied field cooled measurements.

View Article Online
DOI: 10.1039/D5MA01163A

Considering the possible ferroelectric properties of BFO, polarization-electric field (P vs. E) loops, as shown in Supplementary Figure S7, were also measured for all three films. All three films exhibited weak polarization, not fully saturated, likely not reaching ideal BFO behavior due to deposition under vacuum or nitrogen atmosphere. The BFO phases in all three films are likely oxygen deficient which leads to lower ferroelectric properties.[31,47,48] Despite this limitation, sufficient ferroelectric BFO is present in each film to produce measurable ferroelectric hysteresis loops. However, due to the discontinuous nature of the BFO phase, there is no clear path for electrical travel through the CFB matrix, or between the BFO and Nb:STO substrate. The Nitrogen PiM film, shown in Supplementary Figure S7A, has the worst ferroelectric properties due to the most leakage occurring, and as seen in the Supplementary Figure S8, this trend continues until measurement failure. All three films show leakage, and the Nitrogen PiM film is the worst. This is believed to be due to the microstructure; because the majority of the BFO is congregating towards the top of the film, there is little ferroelectric BFO in contact with either the bottom or top electrode. The Vacuum PiM and Bilayer films show better responses, but still no true saturation. Further deposition tuning could be done to minimize the presence of oxygen vacancies, but in the two co-deposited microstructures, this would lead to the oxidation and degradation of the CFB phase.

Magnetic characterization indicates that the PiM nanocomposite design of CFB-BFO film offers improved anisotropy when compared to a more traditional Bilayer system, though the deposition parameters need to be carefully controlled to not compromise the ferroelectric properties. Both PiM films showed an increased magnetic saturation at both room temperature and low temperature, and at room temperature, the coercivities of the films were all comparable. The PiM films also showed greater exchange coupling than the Bilayer film. These enhancements are

View Article Online
DOI: 10.1039/D5MA01163A

attributed to the different microstructures seen in the PiM film, particularly with the BFO nanoparticle arrangement throughout the film. These advantages are achieved through the one-step co-deposition method used for PiM growth which resulted in better CFB growth when compared to the Bilayer film using our PLD deposition parameters. Further tuning of the Bilayer deposition parameters could improve this growth, but it would still lack the increased material interfaces from the PiM microstructure. Most importantly, the microstructures of these composite films suggest that this system is sensitive to deposition parameters, i.e., small changes in the deposition parameters can lead to large microstructure changes and significantly affect the properties. On the other hand, this is the first demonstration of co-growth of CFB and BFO based nanocomposites.

Similar BFO-based nanocomposites explored previously include BFO-$CoFe_2O_4$ (CFO), BFO-MgO, and BFO-$MgAl_2O_4$ (MAO) all having been deposited previously to take advantage of BFO's ferroelectric properties with other materials, with CFO being one of the most common material materials for co-growth due to the capabilities of CFO-BFO films to form new two-phase multiferroic films.[49–52] Due to CFO already being a stronger ferromagnetic material, antiferromagnetic-ferromagnetic exchange coupling could still occur in the CFO-BFO system. Future investigation with this new CFB-BFO nanocomposite could include optimizing for the ferroelectric properties or testing these materials for their potential in spintronic applications. Further study on magnetic damping properties of the CFB-BFO nanocomposites could also be beneficial for future ferroelectric spintronic applications. Another possible direction could be using doped BFO such as $BiFe_{0.7}Mn_{0.3}O$, which is antiferromagnetic with some internal ferromagnetic domain, possibly allowing for improved coupling.[53] Beyond BFO, other multiferroic materials, especially those with stronger ferroelectric properties, such as $BaFe_{11.9}In_{0.1}O_{19}$ and $BaFe_{12-x}Al_xO_{19}$,

View Article Online
DOI: 10.1039/D5MA01163A

could be studied.[54,55] Unfortunately, these mentioned materials are ferromagnetic, losing out on the AFM-FM exchange coupling present in the CFB-BFO nanocomposite.

View Article Online
DOI: 10.1039/D5MA01163A

Conclusion

This work presents the first experimental demonstration of CoFeB (CFB)-$BiFeO_3$ (BFO) particle-in-matrix (PiM) nanocomposites, which were compared against a more conventional CFB-BFO Bilayer film. Two different PiM films were deposited under different deposition conditions, resulting in inverted microstructures confirming that this material system is sensitive to deposition parameters. The two PiM films showed increased magnetic saturation, and a stronger exchange bias compared to the Bilayer film, showing the benefit of the PiM microstructure due to the co-deposition of CFB and BFO and allowing for better growth of the CFB phase along with increased material interfaces between CFB and BFO under the growth condition employed in the PLD experiments. The comparison of magnetic properties between bilayer films and PiM is hindered by the fact that the bilayer film was optimized for crystallinity instead of for its magnetic properties. A more extensive study consisting of improving deposition parameters on a more common substrate for CoFeB growth, such as Si, could allow for a fairer comparison, and better potential future applications by allowing for easier device integration. Ferroelectric properties were also observed in all films despite the obvious leakage due to oxygen deficient growth conditions, with further work necessary for improving this property. The combined ferromagnetic and ferroelectric properties suggest that this co-deposition of CFB-BFO PiM nanocomposites has potential for multiple applications ranging from ferroelectric random access memory (FeRAM) to ferroelectric spintronics.

View Article Online
DOI: 10.1039/D5MA01163A

Experimental Methods

The BFO ($BiFeO_3$) targets were prepared from bismuth oxide (Bi_2O_3) and iron oxide (Fe_2O_3) powders, pressed into a 2 inch target, and sintered at 700°C for 10 hours. For the particle in matrix (PiM) depositions, one target was cut into pie-pieces while the other was kept whole. The CFB (CoFeB) target was mixed from Co, Fe, and B powders, and sintered using spark plasma sintering (SPS) at 600°C for 10 minutes. This was kept whole as it was used as the base of the pie-shaped target. The films were deposited using pulsed laser deposition (PLD) with a KrF excimer laser (Lambda Physik, λ=248 nm). The Nitrogen PiM film was deposited at 550°C, an atmosphere of 50 mTorr N_2, a laser energy of 500 mJ, laser frequency of 5 Hz, and 5000 pulses. The Vacuum PiM film was deposited at 600°C, a vacuum atmosphere (at least $3x10^{-6}$ Torr or better), laser energy of 450 mJ, laser frequency of 5 Hz, and 5000 pulses. The target used for the two PiM films was a pie-shaped target with a CFB base and BFO pie-pieces on top. The ratio between materials during the deposition was kept consistent at 50-50. The Bilayer film was deposited at 600°C, atmosphere of 50 mTorr N_2, laser energy of 450 mJ, laser frequency of 5 Hz, then a deposition pattern of 6000 pulses on the CFB target followed by 4000 pulses on the BFO target. All films were cooled to room temperature after deposition at 15°C/minute in the same atmosphere as the deposition. All films were deposited on $SrTiO_3$ (STO) substrates for XRD, TEM, and magnetic hysteresis measurements, and all films were deposited on Nb:STO substrates as the bottom electrode for electrical hysteresis measurements.

Characterization to confirm the crystallinity, elemental, and microstructural qualities of the thin film samples was done with an PANalytical Empyrean XRD with a Cu Kα radiation source and a high-resolution Thermo Fisher Scientific TALOS 200× with TEM and STEM operated at 200 kV. With a FEI Titan™ G2 80-200 STEM with a Cs probe corrector and ChemiSTEM™

View Article Online
DOI: 10.1039/D5MA01163A

technology (X-FEG™ and SuperX™ energy-dispersive X-ray spectroscopy (EDS) with four windowless silicon drift detectors) also operated at 200 kV, STEM and EDS could be performed on the samples. Sample preparation for all samples was done by hand by thinning the sample through manual grinding and polishing. Dimpling and polishing made a thin area in the center of the sample, and the sample preparation was completed with a Gatan PIPS II Model 695 ion miller.

Magnetic hysteresis measurements were completed with an MPMS Model 3 (Quantum Design) with EverCool SQUID magnetometer in the user facility of the Birck Nanotechnology Center at Purdue University see birck.research.purdue.edu . The magnetic moment versus applied field measurement was completed at both 300 K and 10 K up to a field of ±50 kOe in both the in-plane and out-of-plane direction. To test for antiferromagnetic-ferromagnetic exchange coupling, the sample was cooled 10 K under an applied field of ±10, ±20, or ±30 kOe. Between each field set (10, 20, 30 kOe) the sample was heated to above the Néel temperature in a furnace and held there for 30 minutes before cooling to fully relax the spins. In the MPMS 3, before each measurement, the sample was heated to 400 K and kept there for 15 minutes to partially relax the spins, then cooled to 10 K under the selected field. After reaching 10 K, the field was first brought to zero before performing the out-of-plane ±50 kOe hysteresis loop. The field was then brought back to zero and the sample back to room temperature. The positive applied field was measured before the negative applied field of the same strength, i.e., +10 kOe first, then -10 kOe, the sample was only heated to 400 K between the positive and negative applied field of the same strength. Corrections for the film thickness (emu/cm^3) were done using the full film thickness and not based only on the ferromagnetic CoFeB material thickness. Magnetic moment versus temperature measurements were done after the exchange bias measurements, still in the MPMS 3. The samples were heated to 400 K in the MPMS and held there for 30 minutes under zero applied field. They

View Article Online
DOI: 10.1039/D5MA01163A

were then cooled to 8 K under zero applied field. The measurement field, 1000 Oe, was then applied and the sample was heated up to 400 K while the ZFC data was collected. The sample was then cooled back to 8 K under the same measurement field while collecting the FC data. The samples were corrected for film thickness (emu/cm3) in the same manner as in the hysteresis loop, then normalized based off of the minimum and maximum measured magnetic moment for each sample.

Ferroelectric hysteresis loops were completed using the Radiant Technologies Precision LC II Ferroelectric Tester. The bottom electrode was Nb:STO and the top electrode was sputtered platinum with an area of $3x10^{-4}$ cm^2. The measurement was done with a period of 0.1 ms, and was performed starting at zero, going to the positive drive voltage, back to zero, negative drive voltage, and ending at zero. The measurements were performed in two locations on the samples from 0.1 V until failure in steps of 0.1 V.

View Article Online
DOI: 10.1039/D5MA01163A

Data Availability

The data supporting this article have been included as part of the Supplementary Information.

Conflicts of Interest

There are no conflicts of interest to declare.

Author contributions

Lizabeth Quigley – Conceptualization, lead; Investigation, lead; Methodology, lead; Investigation, lead; Project administration, lead; Validation, lead; Visualization, lead; Writing – original draft, lead

Nirali A. Bhatt – Investigation, supporting

Katrina Evancho – Investigation, supporting

Jianan Shen – Investigation, supporting

Juanjuan Lu – Investigation, supporting

James P. Barnard – Investigation, supporting

Max Chhabra – Investigation, supporting

Ping Lu – Investigation, supporting

Raktim Sarma – Supervision, supporting

Aleem Siddiqui – Supervision, supporting

Haiyan Wang – Funding acquisition, lead; Resources, lead; Supervision, lead; Writing – review & editing, supporting

View Article Online
DOI: 10.1039/D5MA01163A

Acknowledgements

This work is supported by the U.S. Department of Energy, Office of Science, Basic Energy Sciences under Award DE-SC0020077. This work was also partially supported by the Laboratory Directed Research and Development program at Sandia National Laboratories, and performed, in part, at the Center for Integrated Nanotechnologies, an Office of Science User Facility operated for the U.S. Department of Energy (DOE) Office of Science by Los Alamos National Laboratories and Sandia National Laboratories. Sandia National Laboratories is a multiprogram laboratory managed and operated by National Technology and Engineering Solutions of Sandia, LLC, a wholly owned subsidiary of Honeywell International, Inc., for the U.S. Department of Energy's National Nuclear Security Administration under contract DE-NA0003525. This paper describes objective technical results and analysis. Any subjective views or opinions that might be expressed in the paper do not necessarily represent the views of the U.S. Department of Energy or the United States Government. Additionally, this work was supported by the Sandia National Laboratories Diversity Initiative Fellowship (L.Q. and N.A.B.). The high-resolution STEM work was supported by the U.S. National Science Foundation DMR-2016453. L.Q. also thanks the support from the Purdue University Doctoral Graduate Fellowship for the first two years of her Ph.D. study. N.A.B acknowledges the support from the Purdue University Andrews Graduate Fellowship.

View Article Online
DOI: 10.1039/D5MA01163A

References

(1) Shen, J.; Barnard, J. P.; Wang, H. A New Class of Single-Phase Multiferroics: Bismuth-Based Layered Supercell Oxide Thin Films—Current Progress and Future Perspectives. *APL Materials* **2024**, *12* (4), 040601. https://doi.org/10.1063/5.0201790.

(2) Lu, C.; Hu, W.; Tian, Y.; Wu, T. Multiferroic Oxide Thin Films and Heterostructures. *Applied Physics Reviews* **2015**, *2* (2), 021304. https://doi.org/10.1063/1.4921545.

(3) Vopson, M. M. Fundamentals of Multiferroic Materials and Their Possible Applications. *Critical Reviews in Solid State and Materials Sciences* **2015**, *40* (4), 223–250. https://doi.org/10.1080/10408436.2014.992584.

(4) Picozzi, S.; Ederer, C. First Principles Studies of Multiferroic Materials. *J. Phys.: Condens. Matter* **2009**, *21* (30), 303201. https://doi.org/10.1088/0953-8984/21/30/303201.

(5) Eerenstein, W.; Mathur, N. D.; Scott, J. F. Multiferroic and Magnetoelectric Materials. *Nature* **2006**, *442* (7104), 759–765. https://doi.org/10.1038/nature05023.

(6) Wu, C.-W.; Chen, P.-H.; Chang, T.-C.; Tan, Y.-F.; Lin, S.-K.; Yeh, Y.-H.; Zhang, Y.-C.; Lin, H.-N.; Chang, K.-C.; Yeh, C.-H.; Sze, S. Phase Transformation on HZO Ferroelectric Layer in Ferroelectric Random-Access Memory Induced by x-Ray Irradiation. *Semicond. Sci. Technol.* **2024**, *39* (2), 025002. https://doi.org/10.1088/1361-6641/ad1130.

(7) Nagel, N.; Mikolajick, T.; Kasko, I.; Hartner, W.; Moert, M.; Pinnow, C.-U.; Dehm, C.; Mazure, C. An Overview of FeRAM Technology for High Density Applications. *MRS Proc.* **2000**, *655*, CC1.1.1. https://doi.org/10.1557/PROC-655-CC1.1.1.

(8) Takashima, D. Overview of FeRAMs: Trends and Perspectives. In *2011 11th Annual Non-Volatile Memory Technology Symposium Proceeding*; 2011; pp 1–6. https://doi.org/10.1109/NVMTS.2011.6137107.

View Article Online
DOI: 10.1039/D5MA01163A

(9) Garcia, V.; Bibes, M.; Bocher, L.; Valencia, S.; Kronast, F.; Crassous, A.; Moya, X.; Enouz-Vedrenne, S.; Gloter, A.; Imhoff, D.; Deranlot, C.; Mathur, N. D.; Fusil, S.; Bouzehouane, K.; Barthélémy, A. Ferroelectric Control of Spin Polarization. *Science* **2010**, *327* (5969), 1106–1110. https://doi.org/10.1126/science.1184028.

(10) Liu, M.; Zhang, L.; Liu, J.; Wan, T. L.; Du, A.; Gu, Y.; Kou, L. Density Functional Theory Studies on Magnetic Manipulation in NiI2 Layers. *ACS Appl. Electron. Mater.* **2023**, *5* (2), 920–927. https://doi.org/10.1021/acsaelm.2c01479.

(11) Xu, Z.; Xue, X.; Zhang, Z.; Mao, B.; Li, R.; Gao, W.; Guo, H.; Lu, H.; Li, H.; Wang, J. Electrical Control of Spin Polarization in a Multiferroic Heterojunction Based on One-Dimensional Chiral Hybrid Metal Halide. *ACS Nano* **2025**, *19* (12), 12033–12040. https://doi.org/10.1021/acsnano.4c17686.

(12) Bilzer, C.; Devolder, T.; Kim, J.-V.; Counil, G.; Chappert, C.; Cardoso, S.; Freitas, P. P. Study of the Dynamic Magnetic Properties of Soft CoFeB Films. *Journal of Applied Physics* **2006**, *100* (5), 053903. https://doi.org/10.1063/1.2337165.

(13) Manuilov, S. A.; Grishin, A. M.; Munakata, M. Ferromagnetic Resonance, Magnetic Susceptibility, and Transformation of Domain Structure in CoFeB Film with Growth Induced Anisotropy. *Journal of Applied Physics* **2011**, *109* (8), 083926. https://doi.org/10.1063/1.3559732.

(14) Jen, S. U.; Yao, Y. D.; Chen, Y. T.; Wu, J. M.; Lee, C. C.; Tsai, T. L.; Chang, Y. C. Magnetic and Electrical Properties of Amorphous CoFeB Films. *Journal of Applied Physics* **2006**, *99* (5), 053701. https://doi.org/10.1063/1.2174113.

(15) Ikeda, S.; Miura, K.; Yamamoto, H.; Mizunuma, K.; Gan, H. D.; Endo, M.; Kanai, S.; Hayakawa, J.; Matsukura, F.; Ohno, H. A Perpendicular-Anisotropy CoFeB–MgO

View Article Online
DOI: 10.1039/D5MA01163A

Magnetic Tunnel Junction. *Nature Mater* **2010**, *9* (9), 721–724. https://doi.org/10.1038/nmat2804.

(16) Sato, H.; Yamanouchi, M.; Miura, K.; Ikeda, S.; Koizumi, R.; Matsukura, F.; Ohno, H. CoFeB Thickness Dependence of Thermal Stability Factor in CoFeB/MgO Perpendicular Magnetic Tunnel Junctions. *IEEE Magnetics Letters* **2012**, *3*, 3000204–3000204. https://doi.org/10.1109/LMAG.2012.2190722.

(17) Silva, A. S.; Sá, S. P.; Bunyaev, S. A.; Garcia, C.; Sola, I. J.; Kakazei, G. N.; Crespo, H.; Navas, D. Dynamical Behaviour of Ultrathin [CoFeB (tCoFeB)/Pd] Films with Perpendicular Magnetic Anisotropy. *Sci Rep* **2021**, *11* (1), 43. https://doi.org/10.1038/s41598-020-79632-0.

(18) Gayen, A.; Modak, R.; Srinivasan, A.; Srinivasu, V. V.; Alagarsamy, P. Thickness Dependent Magneto-Static and Magneto-Dynamic Properties of CoFeB Thin Films. *Journal of Vacuum Science & Technology A* **2019**, *37* (3), 031513. https://doi.org/10.1116/1.5091675.

(19) Gokce Polat, E.; Deger, C.; Yildiz, F. Investigation of Ferromagnetic Resonance and Damping Properties of CoFeB. *Current Applied Physics* **2019**, *19* (5), 614–620. https://doi.org/10.1016/j.cap.2019.03.002.

(20) Nayak, S.; Mohanty, S.; Bhusan Singh, B.; Bedanta, S. Magnetic Properties in Soft (CoFeB)/Hard (Co) Bilayers Deposited under Different Ar Gas Pressure. *J. Phys.: Condens. Matter* **2022**, *34* (38), 385801. https://doi.org/10.1088/1361-648X/ac7f72.

(21) Han, Y.; Han, J.; Choi, H. J.; Shin, H.-J.; Hong, J. Microscopic and Electronic Roles of B in CoFeB-Based Magnetic Tunnel Junctions. *J. Mater. Chem.* **2011**, *21* (38), 14967–14970. https://doi.org/10.1039/C1JM12096D.

View Article Online
DOI: 10.1039/D5MA01163A

(22) Liu, H.; Mao, X.; Cui, J.; Jiang, S.; Zhang, W. Investigation of High Temperature Electrical Insulation Property of MgO Ceramic Films and the Influence of Annealing Process. *Ceramics International* **2019**, *45* (18, Part A), 24343–24347. https://doi.org/10.1016/j.ceramint.2019.08.151.

(23) Yamamoto, T.; Ichinose, T.; Uzuhashi, J.; Nozaki, T.; Ohkubo, T.; Yakushiji, K.; Tamaru, S.; Kubota, H.; Fukushima, A.; Hono, K.; Yuasa, S. Perpendicular Magnetic Anisotropy and Its Voltage Control in MgO/CoFeB/Mo/CoFeB/MgO Junctions. *J. Phys. D: Appl. Phys.* **2022**, *55* (27), 275003. https://doi.org/10.1088/1361-6463/ac6634.

(24) An, G.-G.; Lee, J.-B.; Yang, S.-M.; Kim, J.-H.; Chung, W.-S.; Hong, J.-P. Highly Stable Perpendicular Magnetic Anisotropies of CoFeB/MgO Frames Employing W Buffer and Capping Layers. *Acta Materialia* **2015**, *87*, 259–265. https://doi.org/10.1016/j.actamat.2015.01.022.

(25) Catalan, G.; Scott, J. F. Physics and Applications of Bismuth Ferrite. *Advanced Materials* **2009**, *21* (24), 2463–2485. https://doi.org/10.1002/adma.200802849.

(26) Sun, H.; Luo, Z.; Liu, C.; Ma, C.; Wang, Z.; Yin, Y.; Li, X. A Flexible BiFeO3-Based Ferroelectric Tunnel Junction Memristor for Neuromorphic Computing. *Journal of Materiomics* **2022**, *8* (1), 144–149. https://doi.org/10.1016/j.jmat.2021.04.009.

(27) Ishiwara, H. Impurity Substitution Effects in BiFeO3 Thin Films—From a Viewpoint of FeRAM Applications. *Current Applied Physics* **2012**, *12* (3), 603–611. https://doi.org/10.1016/j.cap.2011.12.019.

(28) Sando, D.; Barthélémy, A.; Bibes, M. BiFeO3 Epitaxial Thin Films and Devices: Past, Present and Future. *J. Phys.: Condens. Matter* **2014**, *26* (47), 473201. https://doi.org/10.1088/0953-8984/26/47/473201.

View Article Online
DOI: 10.1039/D5MA01163A

(29) Singh, A.; Khan, Z. R.; Vilarinho, P. M.; Gupta, V.; Katiyar, R. S. Influence of Thickness on Optical and Structural Properties of BiFeO3 Thin Films: PLD Grown. *Materials Research Bulletin* **2014**, *49*, 531–536. https://doi.org/10.1016/j.materresbull.2013.08.050.

(30) Botea, M.; Chirila, C.; Boni, G. A.; Pasuk, I.; Trupina, L.; Pintilie, I.; Hrib, L. M.; Nicu, B.; Pintilie, L. Lead-Free BiFeO3 Thin Film: Ferroelectric and Pyroelectric Properties. *Electronic Materials* **2022**, *3* (2), 173–184. https://doi.org/10.3390/electronicmat3020015.

(31) Yun, K. Y.; Noda, M.; Okuyama, M.; Saeki, H.; Tabata, H.; Saito, K. Structural and Multiferroic Properties of BiFeO3 Thin Films at Room Temperature. *Journal of Applied Physics* **2004**, *96* (6), 3399–3403. https://doi.org/10.1063/1.1775045.

(32) Béa, H.; Bibes, M.; Cherifi, S.; Nolting, F.; Warot-Fonrose, B.; Fusil, S.; Herranz, G.; Deranlot, C.; Jacquet, E.; Bouzehouane, K.; Barthélémy, A. Tunnel Magnetoresistance and Robust Room Temperature Exchange Bias with Multiferroic BiFeO3 Epitaxial Thin Films. *Applied Physics Letters* **2006**, *89* (24), 242114. https://doi.org/10.1063/1.2402204.

(33) Ikeda, S.; Hayakawa, J.; Ashizawa, Y.; Lee, Y. M.; Miura, K.; Hasegawa, H.; Tsunoda, M.; Matsukura, F.; Ohno, H. Tunnel Magnetoresistance of 604% at 300K by Suppression of Ta Diffusion in CoFeB/MgO/CoFeB Pseudo-Spin-Valves Annealed at High Temperature. *Applied Physics Letters* **2008**, *93* (8), 082508. https://doi.org/10.1063/1.2976435.

(34) Martí, X.; Park, B. G.; Wunderlich, J.; Reichlová, H.; Kurosaki, Y.; Yamada, M.; Yamamoto, H.; Nishide, A.; Hayakawa, J.; Takahashi, H.; Jungwirth, T. Electrical Measurement of Antiferromagnetic Moments in Exchange-Coupled IrMn/NiFe Stacks. *Phys. Rev. Lett.* **2012**, *108* (1), 017201. https://doi.org/10.1103/PhysRevLett.108.017201.

(35) Skubic, B.; Hellsvik, J.; Nordström, L.; Eriksson, O. Exchange Coupling and Exchange Bias in FM/AFM Bilayers for a Fully Compensated AFM Interface. *Acta Phys. Pol. A*

View Article Online
DOI: 10.1039/D5MA01163A

2009, *115* (10), 25–29. https://doi.org/10.12693/APhysPolA.115.25.

(36) Yakout, S. M. Spintronics and Innovative Memory Devices: A Review on Advances in Magnetoelectric BiFeO3. *J Supercond Nov Magn* **2021**, *34* (2), 317–338. https://doi.org/10.1007/s10948-020-05764-z.

(37) Shah, J.; Bhatt, P.; Diana Diana Dayas, K.; Kotnala, R. K. Significant Role of Antiferromagnetic GdFeO3 on Multiferroism of Bilayer Thin Films. *Mater. Res. Express* **2018**, *5* (2), 026416. https://doi.org/10.1088/2053-1591/aaab8e.

(38) Greene, J. E. Review Article: Tracing the Recorded History of Thin-Film Sputter Deposition: From the 1800s to 2017. *Journal of Vacuum Science & Technology A* **2017**, *35* (5), 05C204. https://doi.org/10.1116/1.4998940.

(39) Balázsi, K.; Balázsi, C. Application of Sputtered Ceramic TiC/a:C Thin Films with Different Structures by Changing the Deposition Parameters. *International Journal of Applied Ceramic Technology* **2022**, *19* (2), 753–761. https://doi.org/10.1111/ijac.13941.

(40) Misra, S.; Li, L.; Jian, J.; Huang, J.; Wang, X.; Zemlyanov, D.; Jang, J.-W.; Ribeiro, F. H.; Wang, H. Tailorable Au Nanoparticles Embedded in Epitaxial TiO2 Thin Films for Tunable Optical Properties. *ACS Appl. Mater. Interfaces* **2018**, *10* (38), 32895–32902. https://doi.org/10.1021/acsami.8b12210.

(41) Gilbert, S. J.; McGarry, M. P.; Meyerson, M. L.; Kotula, P. G.; Yates, L.; Ohlhausen, J. A.; Sharma, P. A.; Trofe, A.; Siegal, M. P.; Biedermann, L. B. Structural, Chemical, and Electronic Control in Co–SiNx Granular Metals for High-Pass Filter Applications. *Journal of Applied Physics* **2025**, *137* (6), 065101. https://doi.org/10.1063/5.0238917.

(42) Song, J.; Wang, H. A Material Design Guideline for Self-Assembled Vertically Aligned Nanocomposite Thin Films. *J. Phys. Mater.* **2025**, *8* (1), 012002.

View Article Online
DOI: 10.1039/D5MA01163A

https://doi.org/10.1088/2515-7639/ad9bee.

(43) Tamion, A.; Raufast, C.; Hillenkamp, M.; Bonet, E.; Jouanguy, J.; Canut, B.; Bernstein, E.; Boisron, O.; Wernsdorfer, W.; Dupuis, V. Magnetic Anisotropy of Embedded Co Nanoparticles: Influence of the Surrounding Matrix. *Phys. Rev. B* **2010**, *81* (14), 144403. https://doi.org/10.1103/PhysRevB.81.144403.

(44) Yamanouchi, M.; Jander, A.; Dhagat, P.; Ikeda, S.; Matsukura, F.; Ohno, H. Domain Structure in CoFeB Thin Films With Perpendicular Magnetic Anisotropy. *IEEE Magnetics Letters* **2011**, *2*, 3000304–3000304. https://doi.org/10.1109/LMAG.2011.2159484.

(45) Huang, J.; Gellatly, A.; Kauffmann, A.; Sun, X.; Wang, H. Exchange Bias Effect along Vertical Interfaces in La0.7Sr0.3MnO3:NiO Vertically Aligned Nanocomposite Thin Films Integrated on Silicon Substrates. *Crystal Growth & Design* **2018**. https://doi.org/10.1021/acs.cgd.8b00366.

(46) Trukhanov, S. V.; Trukhanov, A. V.; Vasiliev, A. N.; Balagurov, A. M.; Szymczak, H. Magnetic State of the Structural Separated Anion-Deficient La0.70Sr0.30MnO2.85 Manganite. *J. Exp. Theor. Phys.* **2011**, *113* (5), 819–825. https://doi.org/10.1134/S1063776111130127.

(47) Scott, J. F. Ferroelectrics Go Bananas. *J. Phys.: Condens. Matter* **2007**, *20* (2), 021001. https://doi.org/10.1088/0953-8984/20/02/021001.

(48) Trukhanov, S. V.; Trukhanov, A. V.; Vasiliev, A. N.; Szymczak, H. Frustrated Exchange Interactions Formation at Low Temperatures and High Hydrostatic Pressures in La0.70Sr0.30MnO2.85. *J. Exp. Theor. Phys.* **2010**, *111* (2), 209–214. https://doi.org/10.1134/S106377611008008X.

(49) Comes, R.; Liu, H.; Khokhlov, M.; Kasica, R.; Lu, J.; Wolf, S. A. Directed Self-Assembly

View Article Online
DOI: 10.1039/D5MA01163A

of Epitaxial CoFe2O4–BiFeO3 Multiferroic Nanocomposites. *Nano Lett.* **2012**, *12* (5), 2367–2373. https://doi.org/10.1021/nl3003396.

(50) Salamon, W.; Gondek, Ł.; Kanak, J.; Sikora, M.; Pawlak, J.; Szuwarzyński, M.; Krawczyk, P. A.; Perzanowski, M.; Maćkosz, K.; Żywczak, A. Self-Assembled Epitaxial BiFeO3 Nanostructures as a Tailored Platform for Vertically Aligned Nanocomposites Development. *Applied Surface Science* **2023**, *607*, 154928. https://doi.org/10.1016/j.apsusc.2022.154928.

(51) Wang, Z.; Li, Y.; Viswan, R.; Hu, B.; Harris, V. G.; Li, J.; Viehland, D. Engineered Magnetic Shape Anisotropy in BiFeO3–CoFe2O4 Self-Assembled Thin Films. *ACS Nano* **2013**, *7* (4), 3447–3456. https://doi.org/10.1021/nn4003506.

(52) Kim, D. H.; Sun, X.; Kim, T. C.; Eun, Y. J.; Lee, T.; Jeong, S. G.; Ross, C. A. Magnetic Phase Formation in Self-Assembled Epitaxial BiFeO3–MgO and BiFeO3–MgAl2O4 Nanocomposite Films Grown by Combinatorial Pulsed Laser Deposition. *ACS Appl. Mater. Interfaces* **2016**, *8* (4), 2673–2679. https://doi.org/10.1021/acsami.5b10676.

(53) Karpinsky, D. V.; Silibin, M. V.; Latushka, S. I.; Zhaludkevich, D. V.; Sikolenko, V. V.; Svetogorov, R.; Sayyed, M. I.; Almousa, N.; Trukhanov, A.; Trukhanov, S.; Belik, A. A. Temperature-Driven Transformation of the Crystal and Magnetic Structures of BiFe0.7Mn0.3O3 Ceramics. *Nanomaterials* **2022**, *12* (16), 2813. https://doi.org/10.3390/nano12162813.

(54) Agayev, F. G.; Trukhanov, S. V.; Trukhanov, An. V.; Jabarov, S. H.; Ayyubova, G. Sh.; Mirzayev, M. N.; Trukhanova, E. L.; Vinnik, D. A.; Kozlovskiy, A. L.; Zdorovets, M. V.; Sombra, A. S. B.; Zhou, D.; Jotania, R. B.; Singh, C.; Trukhanov, A. V. Study of Structural Features and Thermal Properties of Barium Hexaferrite upon Indium Doping. *J Therm Anal*

View Article Online
DOI: 10.1039/D5MA01163A

Calorim **2022**, *147* (24), 14107–14114. https://doi.org/10.1007/s10973-022-11742-5.

(55) Trukhanov, A. V.; Trukhanov, S. V.; Kostishin, V. G.; Panina, L. V.; Salem, M. M.; Kazakevich, I. S.; Turchenko, V. A.; Kochervinskii, V. V.; Krivchenya, D. A. Multiferroic Properties and Structural Features of M-Type Al-Substituted Barium Hexaferrites. *Phys. Solid State* **2017**, *59* (4), 737–745. https://doi.org/10.1134/S1063783417040308.